
Article:
Chen, L., Li, B. and de Borst, R. orcid.org/0000-0002-3457-3574 (2021) The use of Powell-Sabin B-Splines in a higher-order phase-field model for crack kinking. Computational Mechanics, 67 (1). pp. 127-137. ISSN 0178-7675

https://doi.org/10.1007/s00466-020-01923-0

Computational Mechanics manuscript No.
(will be inserted by the editor)

The use of Powell-Sabin B-Splines in a higher-order phase-field model for crack kinking

Lin Chen · Bin Li · René de Borst

Received: date / Accepted: date

Abstract Phase-field models for brittle fracture in anisotropic materials result in a fourth-order partial differential equation for the damage evolution. This necessitates a $\mathcal{C}^1$ continuity of the basis functions. Here, Powell-Sabin B-splines, which are based on triangles, are used for the approximation of the field variables as well as for the the description of the geometry. The use of triangles makes adaptive mesh refinement and discrete crack insertion straightforward. Bézier extraction is used to cast the B-splines in a standard finite element format. A procedure to impose Dirichlet boundary condition is provided for these elements. The versatility and accuracy of the approach are assessed in two case studies, featuring crack kinking and zig-zag crack propagation. It is also shown that the adaptive refinement well captures the evolution of the phase field.

Keywords Phase-field model · Powell-Sabin B-splines · anisotropy · Bézier extraction · adaptive refinement

This research has been supported by the European Research Council under Advanced Grant 664734

Lin Chen
University of Sheffield
Sheffield S1 3JD, UK.
E-mail: lin.chen@sheffield.ac.uk

Bin Li
Cornell University
Ithaca, NY 14853, USA.
E-mail: bl736@cornell.edu

René de Borst
University of Sheffield
Sheffield S1 3JD, UK.
E-mail: r.deborst@sheffield.ac.uk

1 Introduction

The analysis of crack propagation remains a challenging problem which comprises initiation, (unstable) propagation, branching, crack interaction, coalescence and merging. A host of numerical models, which include discrete crack models, phase-field models, and particle methods, have been proposed to model these phenomena, e.g. [1–6].

The phase-field modelling of crack propagation starts from the pioneering works of Francfort and Marigo [7], in which a variational, discontinuity-free formulation has been introduced for brittle fracture. The method relies on a regularised description of the discontinuities [8]. In the regularised model, cracks are represented by a scalar phase-field variable c, which varies smoothly in a band of finite width from 1 for the completely broken material to 0 away from the crack, and thus provides a damage-like description of the crack [9]. For materials with an isotropic surface energy phase-field models have been shown to predict the crack path fairly accurately [10].

Materials with an anisotropic surface energy also exist, either because of their inherent microstructure, or as a consequence of the manufacturing process. Such an anisotropy can strongly influence the crack path, for instance in single crystals, in geological materials, or in extruded polymers. Experimental results clearly show a different crack propagation behaviour from that in materials with an isotropic surface energy [11, 12]. Such materials are characterised by an orientation-dependent fracture toughness $\mathcal{G}_c$.

Distinction is often made between a weakly and a strongly anisotropic surface energy. The latter case is related to phenomena like sawtooth crack patterns or 'forbidden' crack directions [13–15]. The use of a strongly anisotropic surface energy directly leads to a higher-order phase-field model. This necessitates the use of $\mathcal{C}^1$-continuous interpolation functions, which can be achieved, for instance, using meshless approaches [16], or via mixed finite element methods [17].

More recently, isogeometric analysis has been advocated to provide this higher order continuity for the phase field between elements [18], and Non-Uniform Rational B-Splines (NURBS) were used as interpolation functions, and to exactly describe the geometry. A more flexible approach is to use T-splines, which allow for local, adaptive refinement [19–22]. It is, however, less straightforward to introduce an initial crack as a discrete discontinuity in the geometry [23]. In order to represent an initial crack in isogeometric analysis, one has to introduce several subdomains, separated by $\mathcal{C}^0$ lines, or alternatively, to prescribe a phase-field value $c = 1$ along the initial crack [18]. Neither solution is fully satisfactory, while for a strongly anisotropic surface energy model directly prescribing a phase-field value $c = 1$ is even not possible [17]. Employing subdomains separated by $\mathcal{C}^0$ lines is detrimental to the higher-order continuity property of isogeometric analysis. It actually degenerates into a standard finite element method with several 'macroelements' (subdomains). Moreover, a higher-order phase field necessitates a higher-order element continuity [18]. While it is possible to construct a higher-order element continuity

in isogeometric analysis, the introduction of an initial crack needs adaptive refinement of the basis functions, resulting in T-splines [3, 24].

Herein, we exploit $\mathcal{C}^1$-continuous Powell-Sabin B-splines to interpolate the displacements and the phase field. They are based on triangles, which allows a direct, straightforward introduction of the crack path in the physical domain. In a phase-field model, a regularisation length $\ell_c > 0$ is introduced which governs the width of the distributed crack. Typically, ℓ_c has a small, but finite value and several elements are needed to properly capture the phase field over the width. Thus, to resolve an accurate description of the crack topology, adaptive mesh refinement is necessary. Since Powell-Sabin B-splines are based on triangles [25], standard mesh refinement tools can be used, and unlike in isogeometric analysis, the refinement can be done in the physical domain, directly by triangle subdivisions. Moreover, the refinement can be done at each side of a triangle. This is different from isogeometric analysis, where the refinement is performed in the parameter domain. New control points are determined by refinement operators from the parameter space. To facilitate the implementation and to enable casting it in a standard finite element data structure, Bézier extraction has been used [26, 27].

The promising use of Powell-Sabin B-Slines in phase-field problems with material anisotropy once more illustrate the versatility of this discretisation technology, after other successful applications to higher-order problems in mechanics, such as the bending of Kirchhoff-Love plates [26], or gradient damage models [28]. The straightforward application of standard remeshing procedures for triangles in the physical domain and the fact that the higher-order continuity does not break down at the crack tip if a discrete crack method is used, make the method highly competitive compared to other methods that can provide higher-order continuity, such as NURBS, T-splines, or meshless methods for a range of problems that require higher-order continuity of the interpolation.

We start with a concise introduction of phase-field approximations of brittle fracture in anisotropic materials, followed by a review of the construction of Powell-Sabin B-splines. Subsequently, the implementation of adaptive refinement is discussed, as well as the update of the state vector after refinement. Two case studies illustrate the numerical performance of the approach and the capturing of characteristic physical phenomena like crack kinking and zigzag crack propagation.

2 Phase-field approximations of anisotropic fracture

Following the variational approach to brittle fracture [7] we consider a cracked body Ω with prescribed displacements $\hat{\mathbf{u}}$ on Γ_u and tractions $\hat{\mathbf{t}}$ on Γ_t. Defining $\mathcal{W}(\boldsymbol{\varepsilon}(\mathbf{u}))$ as the energy density function, the total energy functional then reads:

$$\mathcal{E}\left(\mathbf{u}, \Gamma\right) = \int_{\Omega\setminus\Gamma} \mathcal{W}(\boldsymbol{\varepsilon}(\mathbf{u}))\, d\Omega - \int_{\Gamma_t} \mathbf{u}\cdot\hat{\mathbf{t}}\, d\Gamma + \int_{\Gamma} \mathcal{G}_c\, d\Gamma \tag{1}$$

We restrict ourselves to small strains and to isotropic linear elasticity, such that $\mathcal{W}(\boldsymbol{\varepsilon}(\mathbf{u})) = \mu\,\boldsymbol{\varepsilon}(\mathbf{u}) \cdot \boldsymbol{\varepsilon}(\mathbf{u}) + \lambda/2\mathrm{tr}(\boldsymbol{\varepsilon}(\mathbf{u}))^{\mathbf{2}}$ with $\boldsymbol{\varepsilon}(\mathbf{u}) = 1/2\left(\nabla\mathbf{u} + \nabla\mathbf{u}^{\mathrm{T}}\right)$, λ and μ are Lamé constants, and $\cdot$ denotes the inner product. The second term in the functional is the potential energy of external forces, while the last term represents the (anisotropic) fracture surface energy in the sense of Griffith's theory of brittle fracture, and Γ is the discontinuity in the displacement field.

Materials with anisotropic fracture properties are described by an orientation-dependent fracture toughness $\mathcal{G}_c = \mathcal{G}_c(\mathbf{n})$, where $\mathbf{n}$ is the unit vector normal to the crack surface. In two dimensions, the vector $\mathbf{n}$ can be replaced by an angle, θ, hence $\mathcal{G}_c(\mathbf{n}) = \mathcal{G}_{\mathbf{c}}(\theta)$. Herein, we partition $\mathcal{G}_c(\theta) = \mathcal{G}_0\,\gamma(\theta)$, where $\mathcal{G}_0$ is a scaling factor with the dimension of energy per unit surface, while $\gamma(\theta)$ represents a dimensionless function. Using this definition, Eq. (1) can be written as:

$$\mathcal{E}\left(\mathbf{u}, \Gamma\right) = \int_{\Omega\setminus\Gamma} \mathcal{W}(\boldsymbol{\varepsilon}(\mathbf{u}))\, d\Omega - \int_{\Gamma_t} \mathbf{u}\cdot\hat{\mathbf{t}}\, d\Gamma + \mathcal{G}_0 \int_{\Gamma} \gamma\left(\theta\right)\, d\Gamma \tag{2}$$

To introduce such an anisotropy in the phase field, higher-order derivatives of the phase-field variable must be included [16]. To make the variational approach to brittle fracture amenable to large-scale computations, the energy functional of Equation (2), which is applicable to a discrete crack, is replaced by the functional [17]:

$$\mathcal{E}_\ell\left(\mathbf{u}, c\right) = \int_{\Omega} a(c)\mathcal{W}(\boldsymbol{\varepsilon}(\mathbf{u}))d\Omega - \int_{\Gamma_t} \mathbf{u}\cdot\hat{\mathbf{t}}d\Gamma + \frac{\mathcal{G}_0}{\beta\ell_c}\int_{\Omega}\left(w(c) + \ell_c^4\nabla^2 c : \mathbf{C} : \nabla^2 c\right) d\Omega \tag{3}$$

where $a(c) = (1-c)^2$ is a degradation function, $w(c) = 9c$ is a monotonically increasing function which represents the energy dissipation per unit volume, and $\beta = 96/5$ is a normalisation parameter. Other choices of $a(c)$ and $w(c)$ could be approached in [29, 30]. $\nabla^2 c$ is a Hessian, i.e. $\left(\nabla^2 c\right)_{ij} = \frac{\partial^2 c}{\partial x_i \partial x_j}$ and $\mathbf{C}$ is a positive-definite fourth-order tensor with the same symmetries as the linear elastic stiffness tensor [31]. Assuming a cubic symmetry, three material constants, C_{1111}, C_{1122} and C_{1212}, suffice to define $\mathbf{C}$.

In the variational approach, the governing equations for the damage evolution problem are given as [4]:

$$\mathrm{div}\,\boldsymbol{\sigma} + \mathbf{b} = 0 \quad \text{in} \quad \Omega, \quad \boldsymbol{\sigma}\cdot\mathbf{n} = \hat{\mathbf{t}} \quad \text{on} \quad \Gamma_t, \tag{4}$$

with $\mathbf{b}$ the body force in Ω and $\hat{\mathbf{t}}$ the traction on Γ_t. In a two-dimensional setting, the damage evolution equation is given as:

$$\begin{aligned}\frac{2\ell_c^3\mathcal{G}_0}{\beta}\left(2\left(C_{1122}+2C_{1212}\right)\frac{\partial^4 c}{\partial x^2\partial y^2} + C_{1111}\left(\frac{\partial^4 c}{\partial x^4} + \frac{\partial^4 c}{\partial y^4}\right)\right)\\ + \mathcal{W}(\boldsymbol{\varepsilon}(\mathbf{u}))\,a'(c) + \frac{\mathcal{G}_0}{\beta}\frac{w'(c)}{\ell_c} = 0\end{aligned} \tag{5}$$

with $(\cdot)' = \mathrm{d}\left(\cdot\right)/\mathrm{d}c$.

The solution of the boundary-value problem must simultaneously satisfy the equilibrium Equation (4) and the damage evolution Equation (5), but also the irreversibility condition $\dot{c} \geq 0$. The latter is enforced by adding a penalty term to Equation (3) [32, 33]:

$$\mathcal{E}_p(c) = \frac{\lambda}{2} \int_\Omega \langle c - c_{n-1} \rangle_-^2 \, d\Omega \quad \text{with} \quad \lambda \gg \frac{\mathcal{G}_0}{\beta \ell_c} \tag{6}$$

which implies $c \geqslant c_{n-1}$, c_{n-1} denoting the phase-field value from the previous step, and $\langle x \rangle_- = \min(0, x)$.

If we consider a two-dimensional setting and a smeared version of a straight crack of orientation θ with respect to the material reference frame, we could obtain the anisotropic surface energy $\mathcal{G}_c(\theta)$ and the effective internal length $\ell(\theta)$ [16, 17]

$$\mathcal{G}_c(\theta) = \mathcal{G}_0 \sqrt[4]{C(\theta)}, \quad \ell(\theta) = \ell_c \sqrt[4]{C(\theta)}, \tag{7}$$

with

$$C(\theta) = \frac{3C_{1111} + C_{1122} + 2C_{1212}}{4} \left(1 + \frac{C_{1111} - C_{1122} - 2C_{1212}}{3C_{1111} + C_{1122} + 2C_{1212}} \cos 4\theta \right). \tag{8}$$

By suitably setting the material constants in $\mathbf{C}$, one can obtain $\mathcal{G}_c(\theta) + \mathcal{G}_c{}''(\theta) < 0$ for a certain range of angles. If the function $\mathcal{G}_c(\theta)$ is convex, the surface energy is called weakly anisotropic, otherwise strongly anisotropic [16, 17]. The convexity can be checked graphically by the convexity of the polar plot of the reciprocal function, $1/\mathcal{G}_c(\theta)$, see Figures 3(a) and 5(b).

In Equation (3) an internal length scale $\ell_c > 0$ has been introduced, which governs the width of the distributed crack. Typically, ℓ_c has a small value and several (Lagrangian) elements are needed to properly capture the strain profile over the crack width. This usually leads to very fine meshes with a concomitant computational burden. A significant advantage can thus be gained by using adaptive mesh refinement, where the advantage of Powell-Sabin B-Splines, which are based on triangles and exploit standard remeshing techniques in the physical domain, offer advantages.

Furthermore, the energy functional Equation (3) of the strongly anisotropy model has the full Hessian of the phase-field variable. A fourth-order partial differential Equation (5) is obtained, thus necessitating $\mathcal{C}^1$ continuity for the interpolation of the phase-field variable. Consequently, the solution space should be constructed such that it allows for a higher-order continuous representation of the phase field. Powell-Sabin B-Splines allow for this, and this is the second reason why they are ideal for modelling phase fields of solids with anisotropic properties.

3 Powell-Sabin B-Splines

We now give a succinct description of Powell-Sabin B-splines [26, 27]. We consider a triangulation $\mathcal{T}$ with $e = 1, 2, \cdots, \mathfrak{L}$ triangles and N_v vertices,

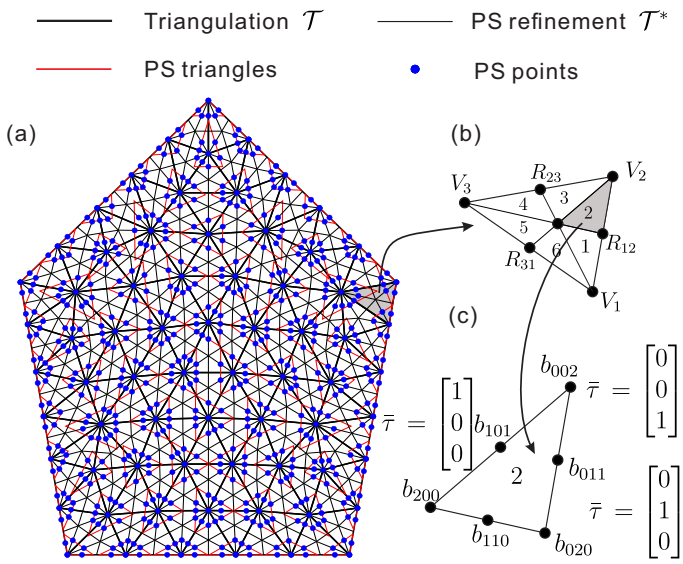

Fig. 1: Example of a triangulation $\mathcal{T}$ (thick black lines), Powell-Sabin refinement $\mathcal{T}^*$ (thin black lines) of $\mathcal{T}$, Powell-Sabin triangles (red) and Powell-Sabin points (blue). In (b) each triangle e is subdivided into six mini-triangles. In (c) each mini-triangle has a barycentric coordinate system $\bar{\tau}$.

which is denoted by thick black lines in Figure 1(a). The triangulation $\mathcal{T}$ can be generated by any package for standard triangular elements, such as Gmsh [34]. To construct Powell-Sabin B-splines, which are $\mathcal{C}^1$-continuous, each triangle e is split into six ($n = 1, 2, \cdots, 6$) mini-triangles, cf. Figure 1(b). This results in the Powell-Sabin refinement $\mathcal{T}^*$. For each vertex k of the triangulation $\mathcal{T}$ Powell-Sabin points are given in blue as the vertex itself and points lying at the centre of the edges of $\mathcal{T}^*$. A Powell-Sabin triangle (in red), which contains all the Powell-Sabin points, is defined for each vertex k. Herein, we employ the algorithm of [35] to find the minimum area triangle which encloses the convex polygon defined by the Powell-Sabin points. For the Powell-Sabin triangles on the boundary, we consider the following constraints: (i) for an angle $\gamma < 180°$, two sides of the Powell-Sabin triangle must be aligned with the two boundary edges, and (ii) for an angle $\gamma = 180°$, one side of the Powell-Sabin triangle must be aligned with the boundary edge, see Figure 1(a).

Three Powell-Sabin B-splines N_k^j, $j = 1, 2, 3$, are defined on each vertex k with coordinates $\boldsymbol{V}_k = \left(x_1^k, x_2^k\right)$, i.e. one for each corner of the Powell-Sabin triangle of vertex k. For any vertex $\boldsymbol{V}_k \neq \boldsymbol{V}_l$ we have:

$$N_k^j\left(\boldsymbol{V}_l\right) = 0, \qquad \frac{\partial}{\partial x_1} N_k^j\left(\boldsymbol{V}_l\right) = 0, \qquad \frac{\partial}{\partial x_2} N_k^j\left(\boldsymbol{V}_l\right) = 0, \tag{9}$$

and otherwise

$$N_k^j\left(\boldsymbol{V}_k\right) = \eta_k^j, \qquad \frac{\partial}{\partial x_1} N_k^j\left(\boldsymbol{V}_k\right) = \beta_k^j, \qquad \frac{\partial}{\partial x_2} N_k^j\left(\boldsymbol{V}_k\right) = \gamma_k^j, \tag{10}$$

with

$$\sum_{j=1}^{3} \eta_k^j = 1, \qquad \sum_{j=1}^{3} \beta_k^j = 0, \qquad \sum_{j=1}^{3} \gamma_k^j = 0. \tag{11}$$

The coefficients η_k^j, β_k^j and γ_k^j are obtained by solving the linear system

$$\begin{bmatrix} \eta_k^1 & \eta_k^2 & \eta_k^3 \\ \beta_k^1 & \beta_k^2 & \beta_k^3 \\ \gamma_k^1 & \gamma_k^2 & \gamma_k^3 \end{bmatrix} \begin{bmatrix} x^{k,1} & y^{k,1} & 1 \\ x^{k,2} & y^{k,2} & 1 \\ x^{k,3} & y^{k,3} & 1 \end{bmatrix} = \begin{bmatrix} x^k & y^k & 1 \\ 1 & 0 & 0 \\ 0 & 1 & 0 \end{bmatrix}, \tag{12}$$

in which $\boldsymbol{Q}_k^j = \left(x^{k,j}, y^{k,j}\right)$ are the coordinates of the corner of the Powell-Sabin triangles which are associated with vertex k. With the coefficients η_k^j, β_k^j and γ_k^j, we can compute the Bézier extraction operator $\boldsymbol{C}_n^e$ for mini-triangle n in element e. We denote the Powell-Sabin B-splines associated with mini-triangle n in element e by $\boldsymbol{N}_n^e$, which is then are computed from:

$$\boldsymbol{N}_n^e = \boldsymbol{C}_n^e \boldsymbol{B}, \tag{13}$$

with the six Bernstein polynomials, contained in the vector $\boldsymbol{B}$ [27].

4 Adaptive analysis for crack growth

As in most calculations of phase-field models, a staggered approach is adopted for the solution of the coupled non-linear problem [33]. The problem is split in a 'displacement' sub-problem and a 'damage' sub-problem. At each time, the two sub-problems are solved iteratively until a convergence criterion has been met. The 'displacement' sub-problem is a standard linear elastic problem.

For the 'phase-field' sub-problem, the solution for c is obtained as the minimisation of Eq. (3) for a fixed $\mathbf{u}$:

$$c = \arg \inf_{c \in \mathcal{S}_c} \left\{ \int_\Omega a(c) \mathcal{W}(\boldsymbol{\varepsilon}(\mathbf{u}))\, d\Omega + \frac{\mathcal{G}_0}{\beta \ell_c} \int_\Omega \left(w(c) + \ell_c^4 \nabla^2 c : \mathbf{C} : \nabla^2 c \right)\, d\Omega \right\} \tag{14}$$

subject to $\dot{c} \geq 0$, where $\mathcal{S}_c = \left\{ c \in H^1(\Omega),\, c|\, \Gamma_c = \hat{c} \right\}$, and $\hat{c}$ denotes the prescribed phase field on Γ_c.

With the Powell-Sabin B-splines, the phase field, the phase field gradient and the Hessian matrix of phase field are approximated by:

$$\mathrm{c} = \mathbf{N}_\mathrm{c} \mathbf{c}_i \qquad \nabla \mathrm{d} = \mathbf{B}_\mathrm{c} \mathbf{c}_i \qquad \mathbf{H}\,(\mathrm{c}) = \mathbf{G}_\mathrm{c} \mathbf{c}_i \tag{15}$$

where $\mathbf{c}_i$ represents the phase field degree of freedom and $\mathbf{H}$ denotes the Hessian matrix. The matrices $\mathbf{N}_\mathrm{c}$, $\mathbf{B}_\mathrm{c}$ and $\mathbf{G}_\mathrm{c}$ contain shape functions, their derivatives, and their second derivatives.

Introducing Equation (15) in Equation (14) results in a linear system of equations for the phase field:

$$\mathbf{K}_\mathrm{c} \mathbf{c} = \mathbf{F}_\mathrm{c} \tag{16}$$

where $\mathbf{c}$ is the vector containing all phase field degrees of freedom,

$$\mathbf{K}_{\mathrm{c}} = \int_{\Omega} \left(2\mathcal{W}(\boldsymbol{\varepsilon}(\mathbf{u}))\mathbf{N}_{\mathrm{c}}^{\mathrm{T}}\mathbf{N}_{\mathrm{c}} + \frac{2\mathcal{G}_0\ell_c^3}{\beta}\,\mathbf{G}_{\mathrm{c}}^{\mathrm{T}}\mathbf{C}_{\mathrm{v}}\mathbf{G}_{\mathrm{c}} \right) d\Omega \tag{17}$$

and

$$\mathbf{F}_{\mathrm{c}} = \int_{\Omega} \left(-2\mathcal{W}(\boldsymbol{\varepsilon}(\mathbf{u})) + \frac{9\mathcal{G}_0}{\beta\ell_c} \right) \mathbf{N}_{\mathrm{c}}^{\mathrm{T}}\, d\Omega \tag{18}$$

with $\mathbf{C}_{\mathrm{v}}$ the Voigt notation of $\mathbf{C}$ in Equation (14). Here, the irreversibility condition $\dot{c} \geq 0$ is enforced by Equation (6).

Because of the use of triangles, mesh refinement is relatively standard. We will first present the implementation aspects for the adaptive refinement. Subsequently, the update of the state vector after refinement is addressed.

4.1 Implementation of adaptive refinement

Below we provide a general procedure for phase field modeling employing adaptive refinement:

$\mathcal{S}1$ Solve for the nodal degrees of freedom of the displacement field $\mathbf{u}$ and of the phase field c.

$\mathcal{S}2$ Compute the phase field c at Gauss integration points of each element.

$\mathcal{S}3$ Mark elements for refinement on the basis of $\mathcal{S}2$. Here, we consider the case if any of phase field c at Gauss integration points exceeds a critical threshold c_{cr}, herein chosen as $c_{cr} = 0.2$.

$\mathcal{S}4$ Refine the marked elements. To locally refine the marked triangle elements, we will use the method developed by Funken [36]. The element refinement is conducted until a prescribed smallest element size e_m is reached in the physical domain. If no element needs to be refined, stop the calculation and proceed to next time step. Otherwise return to $\mathcal{S}1$.

4.2 Update of the state vector after refinement

During refinement, new elements and vertices are introduced to better capture the phase field during crack propagation. This evidently results in a modification of the mesh. Hence, Powell-Sabin B-spline functions must be computed on the new triangles. For non-linear problems, this requires a transfer of the state vector, namely the displacement and the phase field, from the previous time t to the new time $t + \Delta t$. We consider the displacement ${}^{t}\mathbf{U}$ and the phase field ${}^{t}\mathbf{c}$, obtained at time t. For the next time $t + \Delta t$, certain elements have been marked for refinement and the Powell-Sabin B-spline basis functions will be updated.

Herein, the bold capital letter refers to vectors related to nodal degrees of freedom, while bold lowercase letter links to the field variable in the domain. In a non-linear solution scheme, we need to map the vectors ${}^{t}\mathbf{U}$ and ${}^{t}\mathbf{c}$ at time step t to produce new initial vectors ${}^{t+\Delta t}_{0}\mathbf{U}$ and ${}^{t+\Delta t}_{0}\mathbf{c}$ at time $t+\Delta t$. We define ${}^{t}\mathbf{N}$ and ${}^{t+\Delta t}\mathbf{N}$ as the Powell-Sabin B-spline functions associated with the mesh before refinement (i.e. Ψ^b) and after refinement (i.e. Ψ^r). Due to the non-interpolatory property of Powell-Sabin B-splines, a least-squares fit is employed to carry out the mapping [37]:

$$\psi = \int_{\Omega} \left\| {}^{t+\Delta t}_{0}\mathbf{w} - {}^{t}\mathbf{w} \right\| \mathrm{d}\Omega = \int_{\Omega} \left\| {}^{t+\Delta t}\mathbf{N}\ {}^{t+\Delta t}_{0}\mathbf{W} - {}^{t}\mathbf{N}\ {}^{t}\mathbf{W} \right\| \mathrm{d}\Omega \tag{19}$$

in which $\mathbf{w}$ contains the field variables, respectively the displacement field $\mathbf{u}$ and the phase field $\mathbf{c}$. $\mathbf{W}$ contains the nodal degrees of freedom. Here, L^2 norm $\|(\cdot)\| = \sqrt{(\cdot)^{\mathrm{T}} \cdot (\cdot)}$.

Minimising Equation (19) with respect to ${}^{t+\Delta t}_{0}\mathbf{W}$ yields:

$$\mathbf{M}\ {}^{t+\Delta t}_{0}\mathbf{W} = \mathbf{p} \tag{20}$$

with

$$\mathbf{M} = \int_{\Psi^r} \left({}^{t+\Delta t}\mathbf{N} \right)^{\mathrm{T}}\ {}^{t+\Delta t}\mathbf{N} \mathrm{d}\Omega \tag{21}$$

which is obtained directly by Gaussian quadrature at each element on the domain Ψ^r after refinement at time step $t+\Delta t$, and

$$\mathbf{p} = \int_{\Psi^b} \left({}^{t+\Delta t}\mathbf{N} \right)^{\mathrm{T}}\ {}^{t}\mathbf{w} \mathrm{d}\Omega = \int_{\Psi^b} \left({}^{t+\Delta t}\mathbf{N} \right)^{\mathrm{T}} \left({}^{t}\mathbf{N} \right)\ {}^{t}\mathbf{W} \mathrm{d}\Omega \tag{22}$$

where the integration is carried out at each element on the domain Ψ^b before refinement at time step t.

Equation (20) could be solved directly by the matrix inverse. To improve the accuracy, we consider the Dirichlet boundary condition.

$$\mathbf{u} = \hat{\mathbf{u}} \qquad \text{on} \qquad \Gamma_u, \qquad\qquad c = \hat{c} \qquad \text{on} \qquad \Gamma_c \tag{23}$$

where Γ_u and Γ_c are boundaries with prescribed displacement and phase field.

5 Case studies

To investigate the performance of the approach, we present two examples with kinked crack path, in a square plate and in a trapezoid specimen, respectively. For the crack propagation direction, it has been suggested that the underlying crack path selection can be related to the GMERR criterion (generalized maximum energy release rate) [38], which postulates that the crack propagate in a direction given by the angle θ such that $\mathcal{G}(\theta)/\mathcal{G}_c(\theta)$ attains a maximum among all $\theta \in [-\pi, \pi]$.

In the first example, we will verify this hypothesis by comparing crack kinking directions in the simulation with the predictions of the GMERR criterion. Adaptive mesh refinement is performed along the crack propagation direction here. In this example, we will also illustrate how to impose Dirichlet boundary conditions in the framework of Powell-Sabin B-Splines.

In the second example, we will investigate zig-zag crack patterns in a trapezoid specimen with a strongly anisotropic surface energy. An initial crack is introduced in the specimen as a discrete discontinuity in the geometry. Using Powell-Sabin B-Splines it can be avoided to introduce subdomains with $\mathcal{C}^0$ lines or to prescribe phase-field values $c = 1$ along the initial crack as has been done using NURBS or T-splines [18].

With a suitable rescaling of the loading [39], we can set the Young modulus $E = 1$ and the scaling surface energy $\mathcal{G}_0 = 1$ for all experiments. Poisson's ratio is set to $\nu = 0.3$. Plane-stress conditions are assumed. The penalty parameter λ in Equation (6) is set equal to $10^4 \times \mathcal{G}_0/\ell_c$. The regularisation length ℓ_c in Equation (3) is given as $\ell_c = 0.02$. We set the smallest element size as $e_m = \ell_c/5$ in the adaptive refinement.

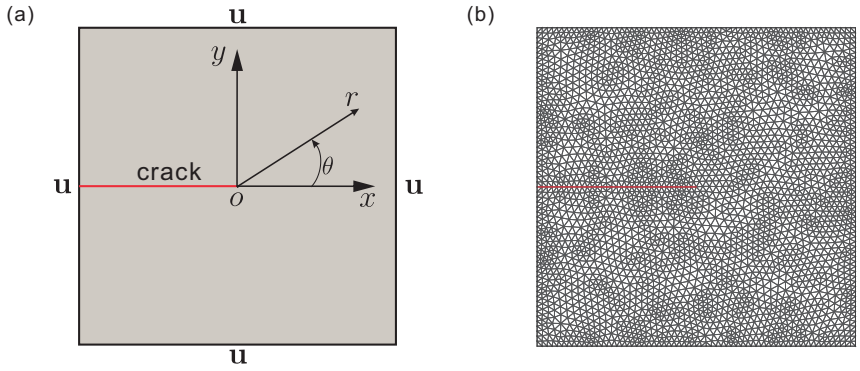

Fig. 2: (a) Geometry and boundary conditions for a square plate. We apply the displacement at the boundary corresponding to the asymptotic crack field with a given mode-I (K_I) stress intensity factor. The initial crack is represented as two overlapping sides; (b) initial triangulation.

5.1 Crack kinking in a square plate

We consider a unit square domain with an initial crack under pure mode-I loading. Figure 2(a) shows the geometry and the boundary conditions. We consider the displacement at the boundary corresponding to the singular stress field (parameterised by the stress intensity factor K_I) around the initial crack tip.

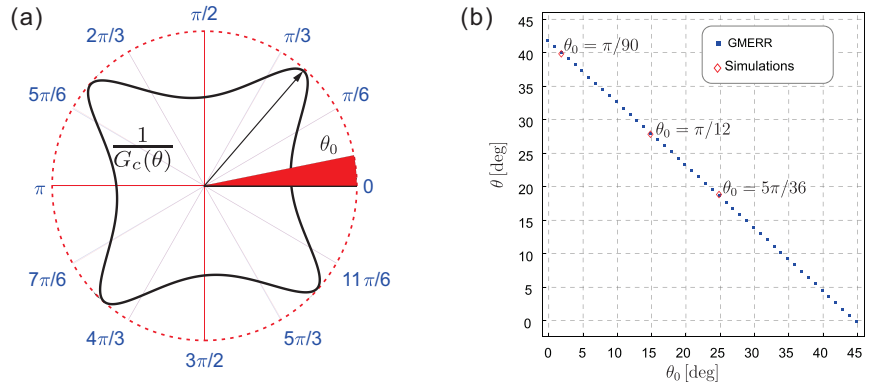

Fig. 3: (a) polar plot of the reciprocal surface energy $1/\mathcal{G}_c(\theta)$, with $\mathcal{G}_c(\theta) = \sqrt[4]{1 + 0.8\cos 4\,(\theta + \theta_0)}$; (b) crack kinking angle predicted by GMERR criterion and phase field simulation.

The analytical expressions of displacement field are recalled in Appendix A. Due to non-interpolatory property of Powell-Sabin B-splines, imposing Dirichlet boundary condition must be carried out by the formulations given in Appendix B. Here, we consider a strongly anisotropic surface energy of the form $\mathcal{G}_c(\theta) = \sqrt[4]{1 + 0.8\cos 4\,(\theta + \theta_0)}$ by setting the parameters $C_{1111} = 1.8$, $C_{1122} = -1.7$ and $C_{1212} = 0.15$ in Eq. (7), and then applying the standard transformation for the rotation of $\mathbf{C}$ by an angle θ_0 [17]. θ_0 denotes the material orientation with respect the x-axis, see Figure 3(a).

Figure 3(b) presents the crack kinking angle θ obtained from the GMERR criterion [17] and the phase-field model. In the figure, different choices of material orientation θ_0 are considered. The results of the phase-field simulations well match those of the GMERR criterion. The predicted crack paths on an adaptive mesh are presented in Figure 4. The adaptive algorithm well captures the crack kinking behaviour, and well resolves the crack path.

5.2 Zigzag crack propagation in a trapezoid specimen

We consider a trapezoid domain under tensile loads, see Figure 2(a) for the geometry and the boundary conditions. The length of the plate is given as the unit length $L = 1$ with a width varying from $H_1 = 0.4L$ to $H_2 = 0.8L$. We introduce an initial crack in the centre plane with a length $L_1 = 0.16L$. It is defined as a discrete discontinuity in the geometry rather than through the introduction of subdomains or the prescription of a phase-field value $c = 1$. We consider a strongly anisotropic surface energy in the form $\mathcal{G}_c(\theta) = \sqrt[4]{1 + 0.8\cos 4\,(\theta + \theta_0)}$. The parameters $C_{1111} = 1.8$, $C_{1122} = -1.7$ and $C_{1212} = 0.15$ are chosen in Equation (7). The rotation of the tensor $\mathbf{C}$ is given by $\theta_0 = \pi/90$, see Figure 5(b).

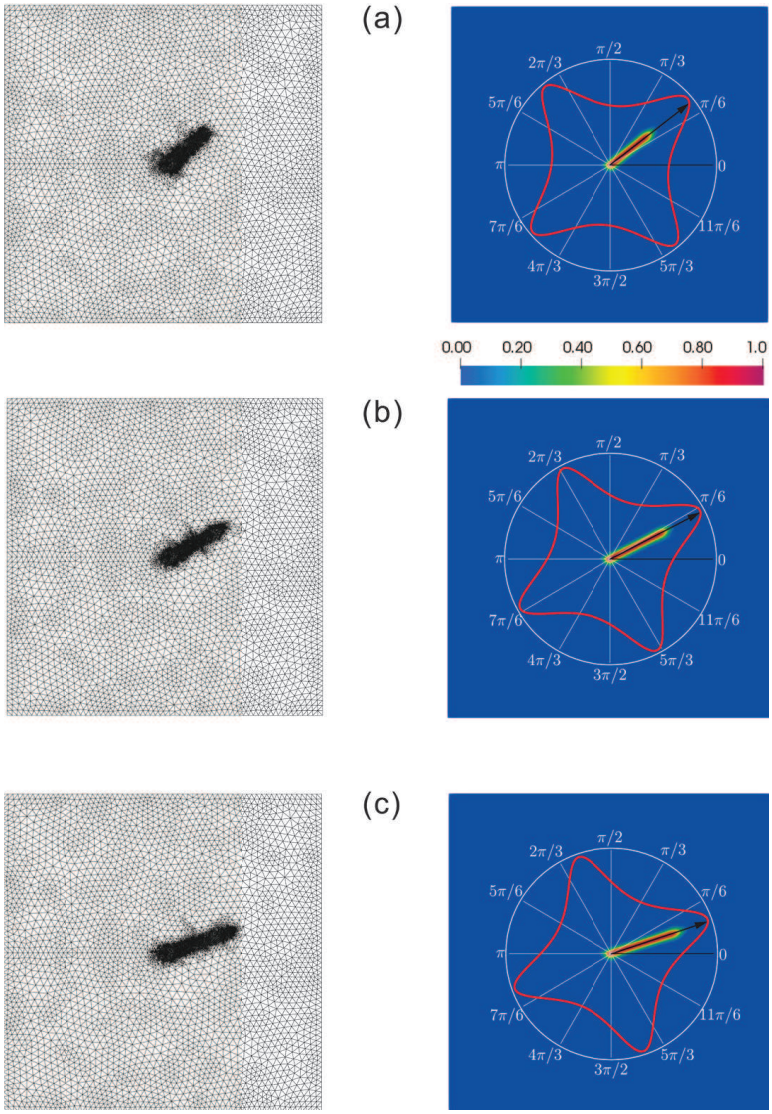

Fig. 4: Meshes for the adaptive refinement (left), and the phase field c (right) under different choice of θ_0. In the figure, the crack direction prediction from the GMERR criterion is also shown and indicated by black arrows. In (a) $\theta_0 = \pi/90$ and GMERR predicts $\theta = 2\pi/9$, in (b) $\theta_0 = \pi/12$ and GMERR predicts $\theta = 7\pi/45$ and in (c) $\theta_0 = 5\pi/36$ and GMERR predicts $\theta = 19\pi/180$.

The specimen is pre-cracked, which provides a stable crack propagation, see Figure 5. In the figure, the Dirichlet boundary conditions are presented, with a zero phase field $c = 0$ and a prescribed displacement $\bar{u}_y$ on the top

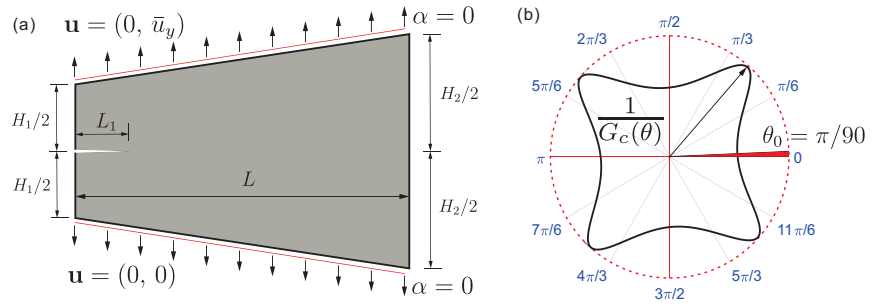

Fig. 5: (a) Geometry and boundary conditions for a trapezoid specimen. In this case the phase-field condition $c = 0$ is imposed on the upper and lower boundaries; (b) polar plot of the reciprocal surface energy $1/\mathcal{G}_c(\theta)$, with $\mathcal{G}_c(\theta) = \sqrt[4]{1 + 0.8\cos 4\,(\theta + \pi/90)}$.

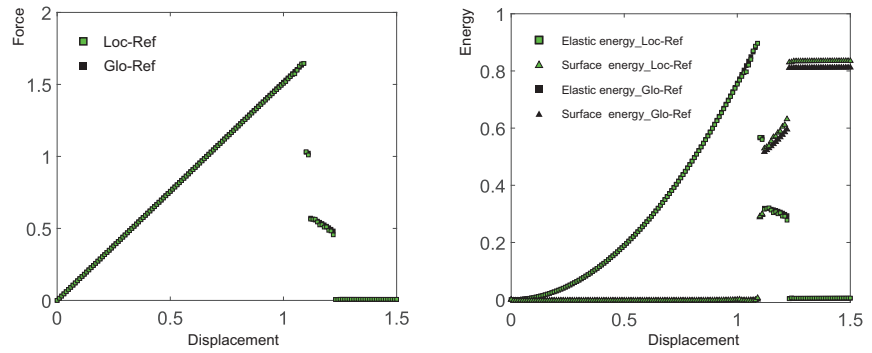

Fig. 6: Load-displacement response and evolution of the elastic and surface energies. The force is obtained by summation of the loads in the y-direction along the top boundary. In the figure, Loc-Ref represents the results of the adaptive refinement, while Glo-Ref stands for those of the global refinement, which are taken as the reference solution.

and the bottom boundaries. A zero phase field boundary condition is enforced to prevent damage at the boundary. Otherwise the crack can propagate along a linear crack path inside the domain and then touch the top boundary. We will therefore not observe a zig-zag crack pattern. A similar crack-guiding protocol has been implemented in [13]. The simulation is operated on a Dell workstation with the Intel Core i9-9980XE processor (18 cores, RAM 128GB). The computation is implemented on Matlab software with parallel coding. The initial mesh has 8984 triangle elements, which yields 46815 triangle elements on the final mesh. The total computation time is 35 days 6 hours 32 minutes. In the computation, most of the time is spent on the update of the state vector after refinement. The refinement is performed at every iteration for each load step. For the state vector update, in the evaluation of Equation (22), we need

to find the state vector of Gauss points on the refined mesh from the old mesh. For each triangle element, there are six mini-triangles used to perform the integration. Therefore, the number of triangles used in the integration of Equation (22) is $N_e \times 6$, and the number of Gauss points on the refined mesh is $N_g \times N_e \times 6$. N_e denotes the total number of triangle elements, N_g is the number of Gauss integration points inside each mini-triangle.

The computed load-displacement curve, as well as the elastic and surface energies are shown in Figure 6. A good agreement is obtained between the solutions of the global and the adaptive refinement. In the figure, the first jump in the force and the energies relates to the re-initiation of the crack associated with an add-crack of a finite length appearing in a single time step [17], see Figure 7(top). The second and the third jumps signify an unstable or brutal crack propagation at each kink [17]. These jumps of the crack are consistent with theoretical analyses [38], which states that a kinking crack must be associated with a jump in time and space of the crack propagation.

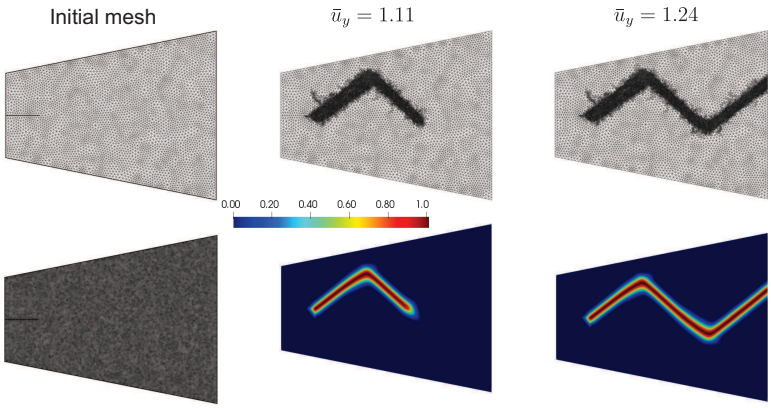

Fig. 7: Meshes for the local (top) refinement, and phase field c (bottom) on a globally refined mesh at different load steps.

6 Concluding remarks

A strongly anisotropic surface energy model has been considered, which can simulate complex crack patterns, including zig-zag crack propagation. For a strongly anisotropy surface energy a higher-order phase field model must be employed, which involves second-order gradient of the phase field in the energy functional. This, in turn, requires $\mathcal{C}^1$ continuity of the intepolation functions in a Continuous Galerkin method.

Powell-Sabin B-splines meet this requirement. They are based on triangles and are $\mathcal{C}^1$ continuous with respect to the interpolation of field variables, also across element boundaries. Remeshing and the introducing of a discrete initial

crack in the physical domain are straightforward. Different from NURBS or T-splines as used in isogeometric analysis, there is no need for reducing the continuity between elements or for prescribing phase-field values $c = 1$ in the domain (which is not well possible when using a strongly anisotropic surface energy model anyway). It once again shows that Powell-Sabin B-Splines are a powerful discretisation method for a range of problems which require $\mathcal{C}^1$-continuity, such as Kirchhoff-Love plates [26] or gradient damage models [28].

Numerical studies reveal an excellent performance of the method. It is shown how to prescribe Dirichlet boundary condition in the case studies. Moreover, the hypothesis is verified that the underlying crack angle selection is determined by the GMERR criterion. The strong anisotropy of the surface energy can involve sudden changes in the crack pattern, with jumps in space and time.

A limitation of Powell-Sabin B-splines regards the extension to three dimensions. No procedure is yet available to define Powell-Sabin B-splines on arbitrary tetrahedral meshes and they currently only work for structured meshes [40].

Acknowledgement

Financial support from the European Research Council (ERC Advanced Grant 664734 PoroFrac) is gratefully acknowledged.

A Crack tip displacement fields

For completeness, we present the formulations of asymptotic displacement fields under pure mode-I loading around a straight crack tip. We impose these displacement fields as boundary conditions to approximate singular stress fields (parameterised by the stress intensity factor $\mathrm{K_I}$) around the crack tip. The asymptotic displacement fields are given as

$$\begin{aligned} u_x &= \frac{\mathrm{K_I}}{2\mu}\sqrt{\frac{r}{2\pi}}\cos\frac{\theta}{2}(\kappa - \cos\theta) \\ u_y &= \frac{\mathrm{K_I}}{2\mu}\sqrt{\frac{r}{2\pi}}\sin\frac{\theta}{2}(\kappa - \cos\theta) \end{aligned} \tag{A.1}$$

where $\mu = E/2(1+\nu)$, $\kappa = 3 - 4\nu$ for plane strain and $\kappa = (3-\nu)/(1+\nu)$ for plane stress, and (r, θ) are polar coordinates with origin positioned at the crack tip. The derivatives of displacement fields with respect to Cartesian coordinates (x, y) at the crack tip read:

$$\begin{aligned} \frac{\partial u_x}{\partial x} &= \frac{\mathrm{K_I}}{4\mu\sqrt{2\pi r}}\cos\frac{\theta}{2}\,(-\cos\theta + \cos 2\theta + \kappa - 1) \\ \frac{\partial u_x}{\partial y} &= \frac{\mathrm{K_I}}{4\mu\sqrt{2\pi r}}\sin\frac{\theta}{2}\,(\cos\theta + \cos 2\theta + \kappa + 1) \\ \frac{\partial u_y}{\partial x} &= \frac{\mathrm{K_I}}{4\mu\sqrt{2\pi r}}\sin\frac{\theta}{2}\,(\cos\theta + \cos 2\theta - \kappa - 1) \\ \frac{\partial u_y}{\partial y} &= \frac{\mathrm{K_I}}{4\mu\sqrt{2\pi r}}\cos\frac{\theta}{2}\,(\cos\theta - \cos 2\theta + \kappa - 1) \end{aligned} \tag{A.2}$$

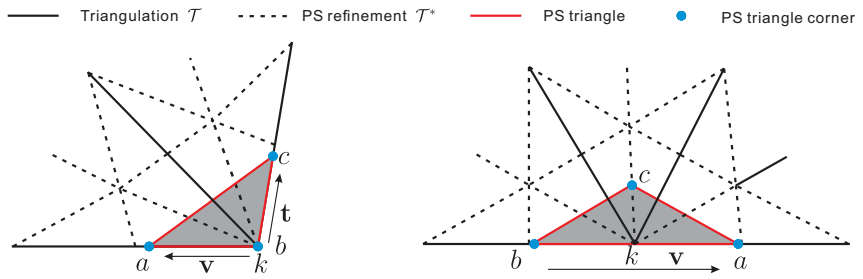

Fig. 8: Imposing Dirichlet boundary conditions to the corners of a Powell-Sabin triangle on boundary vertices with: an angle different from π (left) and equal to π (right).

B Imposing Dirichlet boundary condition

We now show how to impose Dirichlet boundary conditions in the framework of Powell-Sabin elements. In Section 3, a special choice of Powell-Sabin (PS) triangle is defined along the boundary: (i) for vertex k with an angle $\gamma < \pi$, two sides of the Powell-Sabin triangle must be aligned with two boundary edges (Figure 8(left)); (ii) for vertex k with an angle $\gamma = \pi$, one side of the Powell-Sabin triangle must be aligned with the boundary edge, see Figure 8(right). Rewriting Equation (12) with respect to the nodal degrees of freedom U yields

$$\begin{bmatrix} \eta_k^a & \eta_k^b & \eta_k^c \\ \beta_k^a & \beta_k^b & \beta_k^c \\ \gamma_k^a & \gamma_k^b & \gamma_k^c \end{bmatrix} \begin{bmatrix} U^{k,a} \\ U^{k,b} \\ U^{k,c} \end{bmatrix} = \begin{bmatrix} U^k \\ \frac{\partial U^k}{\partial x} \\ \frac{\partial U^k}{\partial y} \end{bmatrix} \tag{B.1}$$

where $U^{k,i}$ is the nodal degrees of freedom of Powell-Sabin triangle corner i $(i = a, b, c)$, associated with vertex k; U^k denotes field values at vertex k; for the example in Section 5.1, U^k is given in Equation (A.1). $\nabla U^k = \begin{bmatrix} \frac{\partial U^k}{\partial x} & \frac{\partial U^k}{\partial y} \end{bmatrix}$ is the gradient of U^k; it is defined in Equation (A.2) for the example in Section 5.1.

For the vertex k with an angle $\gamma < \pi$, the coefficients η_k^i, β_k^i and γ_k^i $(i = a, b, c)$ have the following conditions:

$$\begin{aligned} &\eta_k^a = \eta_k^c = 0, \quad \eta_k^b = 1 \\ &\begin{bmatrix} \beta_k^a \\ \gamma_k^a \end{bmatrix} \cdot \mathbf{t} = 0, \quad \begin{bmatrix} \beta_k^c \\ \gamma_k^c \end{bmatrix} \cdot \mathbf{v} = 0 \end{aligned} \tag{B.2}$$

in which $\mathbf{t}$ and $\mathbf{v}$ are unit vectors along the boundary.

$$\mathbf{t} = \frac{\mathbf{x}_a - \mathbf{x}_b}{\|\mathbf{x}_a - \mathbf{x}_b\|}, \qquad \mathbf{v} = \frac{\mathbf{x}_c - \mathbf{x}_b}{\|\mathbf{x}_c - \mathbf{x}_b\|} \tag{B.3}$$

From Equations (B.1) and (B.2), we obtain:

$$U^{k,b} = U^k, \qquad U^{k,a} = U^k + \frac{\nabla U^k \cdot \mathbf{v}}{\begin{bmatrix} \beta_k^a \\ \gamma_k^a \end{bmatrix} \cdot \mathbf{v}}, \qquad U^{k,c} = U^k + \frac{\nabla U^k \cdot \mathbf{t}}{\begin{bmatrix} \beta_k^c \\ \gamma_k^c \end{bmatrix} \cdot \mathbf{t}} \tag{B.4}$$

For the case of vertex k with an angle $\gamma = \pi$, the coefficients η_k^i, β_k^i and γ_k^i $(i = a, b, c)$ should satisfy

$$\begin{aligned} &\eta_k^a \neq 0, \quad \eta_k^b \neq 0, \quad \eta_k^c = 0 \\ &\begin{bmatrix} \beta_k^c \\ \gamma_k^c \end{bmatrix} \cdot \mathbf{v} = 0 \end{aligned} \tag{B.5}$$

where $\mathbf{v}$ denotes the unit vector along the boundary given in Equation (B.3).

Considering Equations (B.1) and (B.5), this leads to

$$U^{k,a} = \frac{U^k \Delta_1 - \eta_k^b \nabla U^k \cdot \mathbf{v}}{\eta_k^a \Delta_1 - \eta_k^b \Delta}, \qquad U^{k,b} = \frac{-U^k \Delta + \eta_k^a \nabla U^k \cdot \mathbf{v}}{\eta_k^a \Delta_1 - \eta_k^b \Delta}, \tag{B.6}$$

with $\Delta = \begin{bmatrix} \beta_k^a \\ \gamma_k^a \end{bmatrix} \cdot \mathbf{v}$, $\Delta_1 = \begin{bmatrix} \beta_k^b \\ \gamma_k^b \end{bmatrix} \cdot \mathbf{v}$.

References

1. R. de Borst, J. J. C. Remmers, A. Needleman, and M. A. Abellan. Discrete vs smeared crack models for concrete fracture: bridging the gap. *International Journal for Numerical and Analytical Methods in Geomechanics*, 28:583–607, 2004.
2. L. Chen, E. J. Lingen, and R. de Borst. Adaptive hierarchical refinement of nurbs in cohesive fracture analysis. *International Journal for Numerical Methods in Engineering*, 112:2151–2173, 2017.
3. L. Chen, C. V. Verhoosel, and R. de Borst. Discrete fracture analysis using locally refined T-splines. *International Journal for Numerical Methods in Engineering*, 116:117–140, 2018.
4. B. Bourdin, G. A. Francfort, and J. J. Marigo. The variational approach to fracture. *Journal of Elasticity*, 91:5–148, 2008.
5. X. P. Zhou, J. Bi, and Q. H. Qian. Numerical simulation of crack growth and coalescence in rock-like materials containing multiple pre-existing flaws. *Rock Mechanics and Rock Engineering*, 48:1097–1114, 2015.
6. F. Fathi, L. Chen, and R. de Borst. Extended isogeometric analysis for cohesive fracture. *International Journal for Numerical Methods in Engineering*, 2020.
7. G. A. Francfort and J. J. Marigo. Revisiting brittle fracture as an energy minimization problem. *Journal of the Mechanics and Physics of Solids*, 46:1319–1342, 1998.
8. B. Bourdin, G. A. Francfort, and J. J. Marigo. Numerical experiments in revisited brittle fracture. *Journal of the Mechanics and Physics of Solids*, 48:797–826, 2000.
9. R. de Borst and C. V. Verhoosel. Gradient damage *vs* phase-field approaches for fracture: Similarities and differences. *Computer Methods in Applied Mechanics and Engineering*, 312:78–94, 2016.
10. Longfei Wang and Xiaoping Zhou. Phase field model for simulating the fracture behaviors of some disc-type specimens. *Engineering Fracture Mechanics*, page 106870, 2020.
11. P. O. Judt, A. Ricoeur, and G. Linek. Crack path prediction in rolled aluminum plates with fracture toughness orthotropy and experimental validation. *Engineering Fracture Mechanics*, 138:33–48, 2015.
12. A. Ibarra, B. Roman, and F. Melo. The tearing path in a thin anisotropic sheet from two pulling points: Wulff's view. *Soft Matter*, 12:5979–5985, 2016.
13. A. Takei, B. Roman, J. Bico, E. Hamm, and F. Melo. Forbidden directions for the fracture of thin anisotropic sheets: an analogy with the Wulff plot. *Physical Review Letters*, 110:144301, 2013.
14. S Teichtmeister, D Kienle, F Aldakheel, and M-A Keip. Phase field modeling of fracture in anisotropic brittle solids. *International Journal of Non-Linear Mechanics*, 97:1–21, 2017.
15. E. G. Kakouris and S. P. Triantafyllou. Phase-field material point method for dynamic brittle fracture with isotropic and anisotropic surface energy. *Computer Methods in Applied Mechanics and Engineering*, 357:112503, 2019.
16. B. Li, C. Peco, D. Millán, I. Arias, and M. Arroyo. Phase-field modeling and simulation of fracture in brittle materials with strongly anisotropic surface energy. *International Journal for Numerical Methods in Engineering*, 102:711–727, 2015.
17. B. Li and C. Maurini. Crack kinking in a variational phase-field model of brittle fracture with strongly anisotropic surface energy. *Journal of the Mechanics and Physics of Solids*, 125:502–522, 2019.

18. M. J. Borden, C. V. Verhoosel, M. A. Scott, T. J. R. Hughes, and C. M. Landis. A phase-field description of dynamic brittle fracture. *Computer Methods in Applied Mechanics and Engineering*, 217-220:77–95, 2012.
19. M. R. Dörfel, B. Jüttler, and B. Simeon. Adaptive isogeometric analysis by local h-refinement with T-splines. *Computer Methods in Applied Mechanics and Engineering*, 199:264–275, 2010.
20. A. V. Vuong, C. Giannelli, B. Jüttler, and B. Simeon. A hierarchical approach to adaptive local refinement in isogeometric analysis. *Computer Methods in Applied Mechanics and Engineering*, 200:3554–3567, 2011.
21. R. de Borst and L. Chen. The role of Bézier extraction in adaptive isogeometric analysis: Local refinement and hierarchical refinement. *International Journal for Numerical Methods in Engineering*, 113:999–1019, 2018.
22. L. Chen and R. de Borst. Adaptive refinement of hierarchical T-splines. *Computer Methods in Applied Mechanics and Engineering*, 337:220–245, 2018.
23. L. Chen and R. de Borst. Locally refined T-splines. *International Journal for Numerical Methods in Engineering*, 114:637–659, 2018.
24. L. Chen, B. Li, and R. de Borst. Adaptive isogeometric analysis for phase-field modelling of anisotropic brittle fracture. *International Journal for Numerical Methods in Engineering*, 2020.
25. P. Dierckx. On calculating normalized powell-sabin b-splines. *Computer Aided Geometric Design*, 15:61–78, 1997.
26. S. May, J. Vignollet, and R. de Borst. Powell-Sabin B-splines and unstructured standard T-splines for the solution of Kirchhoff-Love plate theory using Bézier extraction. *International Journal for Numerical Methods in Engineering*, 107:205–233, 2016.
27. L. Chen and R. de Borst. Cohesive fracture analysis using Powell-Sabin B-splines. *International Journal for Numerical and Analytical Methods in Geomechanics*, 43:625–640, 2019.
28. S. May, R. de Borst, and J. Vignollet. Powell-Sabin B-splines for smeared and discrete approaches to fracture in quasi-brittle materials. *Computer Methods in Applied Mechanics and Engineering*, 307:193–214, 2016.
29. J. M. Sargado, E. Keilegavlen, I. Berre, and J. M. Nordbotten. High-accuracy phase-field models for brittle fracture based on a new family of degradation functions. *Journal of the Mechanics and Physics of Solids*, 111:458–489, 2018.
30. C. Kuhn, A. Schlüter, and R. Müller. On degradation functions in phase field fracture models. *Computational Materials Science*, 108:374–384, 2015.
31. L. Chen. Three-dimensional Green's function for an anisotropic multi-layered half-space. *Computational Mechanics*, 56:795–814, 2015.
32. T. Gerasimov and L. De Lorenzis. On penalization in variational phase-field models of brittle fracture. *Computer Methods in Applied Mechanics and Engineering*, 354:990–1026, 2019.
33. C. Miehe, F. Welschinger, and M. Hofacker. Thermodynamically consistent phase-field models of fracture: Variational principles and multi-field FE implementations. *International Journal for Numerical Methods in Engineering*, 83:1273–1311, 2010.
34. C. Geuzaine and J. F. Remacle. Gmsh: A 3-D finite element mesh generator with built-in pre-and post-processing facilities. *International Journal for Numerical Methods in Engineering*, 79:1309–1331, 2009.
35. J. O'Rourke, A. Aggarwal, S. Maddila, and M. Baldwin. An optimal algorithm for finding minimal enclosing triangles. *Journal of Algorithms*, 7:258–269, 1986.
36. S. Funken, D. Praetorius, and P. Wissgott. Efficient implementation of adaptive P1-FEM in Matlab. *Computational Methods in Applied Mathematics*, 11:460–490, 2011.
37. L. Chen, B. Li, and R. de Borst. Energy conservation during remeshing in the analysis of dynamic fracture. *International Journal for Numerical Methods in Engineering*, 120:433–446, 2019.
38. A. Chambolle, G. A. Francfort, and J. J. Marigo. When and how do cracks propagate? *Journal of the Mechanics and Physics of Solids*, 57:1614–1622, 2009.
39. P. Farrell and C. Maurini. Linear and nonlinear solvers for variational phase-field models of brittle fracture. *International Journal for Numerical Methods in Engineering*, 109:648–667, 2017.

40. A. J. Worsey and B. Piper. A trivariate Powell-Sabin interpolant. *Computer Aided Geometric Design*, 5:177–186, 1988.